nature communications

Article

https://doi.org/10.1038/s41467-026-68312-8

Exciton-polariton photodiodes

Received: 25 March 2025

Accepted: 2 January 2026

Published online: 17 January 2026

Check for updates

Qixiao Zhao[1,2], Adam D. Alfieri[3], Mengjia Xia[1,2], Anping Ge[1,2], Haonan Ge[1,2], Liaoxin Sun[1,2], Runzhang Xie[1,2], Fang Wang[1,2], Deep Jariwala[3] ✉, Jinshui Miao[1,2] ✉ & Weida Hu[1,2] ✉

Photodiodes are central to high-speed communication, sensing and light-harvesting devices. While silicon and other inorganic semiconductor-based photodiodes have been widely integrated into commercial technologies, photodiodes from excitonic semiconductors continue to maintain high interest in research. Excitonic semiconductors are superior in terms of absorption as compared to silicon and III-V semiconductors, but have always suffered from poor charge transport and narrow band absorption due to the short diffusion lengths and resonant nature of the excitons, respectively. Here, we attempt to solve both these central issues in excitonic photodiode devices via use of polariton physics and demonstrating photodiodes in the strong light-matter coupling regime. By using a conductive tin-doped indium oxide transparent top electrode that also serves as an anti-reflective coating combined with self-trapping and hybridization of light in inorganic excitonic semiconductor WS_2, we demonstrate photodiodes with broadband absorption and internal quantum efficiency values approaching unity near the zero-detuning condition. Furthermore, it is demonstrated that the response speed of photodiodes is enhanced under strong coupling. Our work presents a promising approach to explore the physics and applications of photodiodes based on excitonic semiconductors.

Photodiodes and photovoltaics based on excitonic semiconductors have emerged as a potentially low-cost alternative to conventional semiconductors[1–9], owing to their markedly enhanced absorption coefficients in photon harvesting processes[10–12]. In excitonic photodiodes and photovoltaics (e.g., organic photovoltaics), the excited state (exciton) must diffuse to a heterointerface before being separated into free carriers[13–15]. However, poor exciton transport is often a limiting factor on device efficiency.

Strong coupling between excitons and cavity photons can occur by placing an excitonic material into an optical cavity with a discrete mode in resonance with the exciton energy[16–21]. The resulting hybrid states are called exciton-polaritons (EPs). EPs, in contrast to excitons, can exhibit long-range transport due to a low effective mass and delocalized wavefunction[22–27]. Recently, the utilization of strong coupling in organic semiconductor devices has been demonstrated, leading to longer exciton diffusion lengths and enhanced photocurrent[28–33]. Notably, most of the previously reported studies on organic photovoltaic devices have required external optical cavities for strong light-matter interactions due to the low refractive indices, thus resulting in considerable energy loss from partially transparent metal top reflectors, leading to the inability to obtain state-of-the-art device performance. In contrast, recent advances in open-cavity architectures have demonstrated a viable pathway toward substantial absorption enhancement without such trade-offs[34,35].

Two-dimensional (2D) transition metal dichalcogenides (TMDCs) feature dielectric screening and strong confinement effects that lead to unusually large exciton binding energies in monolayers (>300 meV), but their van der Waals bonding out of plane also ensures binding energies > 25 meV in the bulk. Thus, exciton photophysics governs photoexcited carriers at room temperature[36]. Furthermore, the large

[1]State Key Laboratory of Infrared Physics, Shanghai Institute of Technical Physics, Chinese Academy of Sciences, Shanghai, China. [2]University of Chinese Academy of Sciences, Beijing, China. [3]Department of Electrical and Systems Engineering, University of Pennsylvania, Philadelphia, PA, USA.
✉e-mail: dmj@seas.upenn.edu; jsmiao@mail.sitp.ac.cn; wdhu@mail.sitp.ac.cn

optical constants and strong light-matter interactions enable strong light absorption in the films[37–39]. TMDCs of Mo and/or W, in particular, show simultaneously strong exciton resonances and large optical constants, enabling self-hybridized EPs and providing a natural platform for investigating photon-exciton coupling without the need for external optical cavities[40–42].

Here, we demonstrate a self-hybridized exciton-polariton photodiode with a transparent conductive top electrode also acting as an antireflective coating, enabling strong light-matter coupling with broadband light absorption and polariton-enhanced transport. The strong-coupling effect is observed with large polariton peaks and dispersion behavior in thickness-dependent reflectance spectra. Corresponding polariton peaks are also observed from external quantum efficiency (EQE) spectra, indicating that the EP states enhance the generation of photocurrent. The strong coupling of excitons to cavity photons in the WS_2 absorber layer enhances the internal quantum efficiency (IQE) to near unity. The exciton polariton transport achieved improves the response speed of the diode, obtaining the fastest response time of 217 ns. This work demonstrates that strong light-matter coupling in self-hybridized structures can be used to design polaritonic photodiodes with broadband absorption and polariton-enhanced transport for improved quantum efficiency and response speed.

Results

Device structure and working principle

The exciton-polariton photodiode is shown in Fig. 1a. WS_2 is contacted by a top tin-doped indium oxide (ITO) layer that functions as both an electrode and an anti-reflective coating layer. The thickness of the WS_2 active layer varies from 5 nm to 200 nm. The index contrast between ITO and air enables the ITO to be used as an antireflective coating (ARC). However, the large optical impedance mismatch between the ITO and WS_2 results in a Fresnel reflection coefficient at the interface that can produce Fabry-Perot (FP) cavity modes in the WS_2 layer. The energy of the FP cavity modes depends approximately linearly on the WS_2 thickness, and dipole-dipole interactions between the cavity photons and the WS_2 excitons result in self-hybridized EPs for WS_2 layers of appropriate thicknesses. Therefore, our ITO/WS_2 devices can simultaneously exhibit self-hybridized EPs and strong off-resonance absorption, benefiting from the ARC and high imaginary permittivity of WS_2 above its bandgap.

A representative device optical image and corresponding photocurrent map illustrate that the photocurrents are spatially distributed uniformly over the entire device range. (Fig. 1b, Supplementary Fig. 1). Generally, the transport of energy carriers in solid state materials is determined by their wave function and their interaction with the environment. As shown in Fig. 1c, conventional photodiodes suffer from three primary energy loss mechanisms: i) the photon with energy $E<E_g$ cannot be absorbed by the material; ii) additional kinetic energy loss of the electron-hole pairs; and iii) recombination of electron-hole pairs. These losses stem mainly from poor charge transport and limited bandgap absorption. In contrast, EPs as neutral bosonic quasiparticles can substantially suppress the Coulomb scattering that plagues conventional charge carriers[43]. This suppression leads to longer diffusion lengths and lower scattering rates, thereby opening avenues for enhanced exciton transport and improved overall photoelectric conversion efficiency[44–47]. In exciton-polariton photodiodes, absorption occurs through exciton-polariton states, the physical

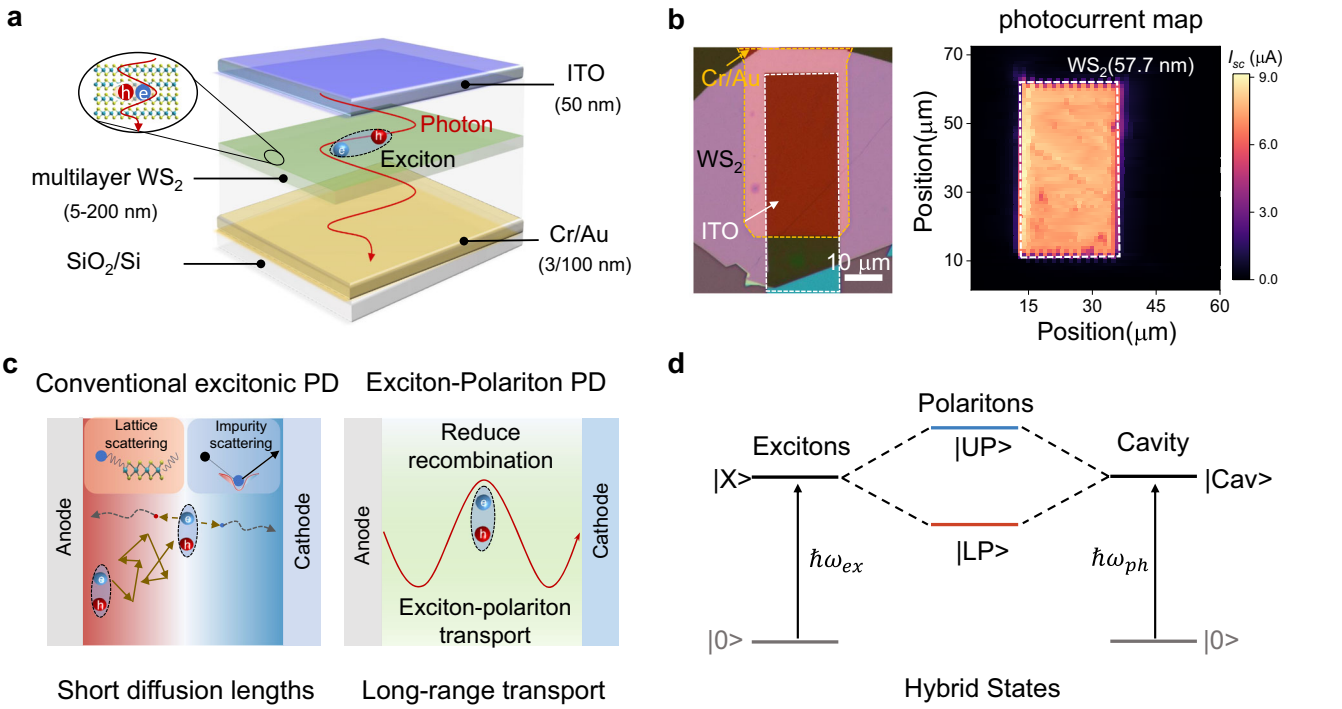

Fig. 1 | Device structure and working principle. a Device structure with multilayer WS_2 between Au and tin-doped indium oxide (ITO). The light reflection between the top and bottom surfaces of WS_2 results in confined photon modes, which are sufficient for strong coupling with the excitons. **b** Photocurrent mapping of the device (excitation wavelength: 633 nm; spot size: ~2 μm; laser power: ~40 μW). The yellow dashed lines outline the Cr/Au electrodes, and the white dashed lines indicate the ITO top contact. I_{sc} denotes the short-circuit photocurrent. **c** Schematic illustration of exciton-polariton photodiode device operation. In the conventional excitonic photodiodes (PD) (left), the random brown arrows indicate exciton transport limited by scattering, resulting in short diffusion lengths. In the exciton-polariton PD (right), the smooth arrowed path represents exciton-polariton transport with reduced recombination, enabling long-range transport. **d** Excited-state diagram illustrating the splitting of the first singlet excited state into two polariton states corresponding to the high-energy upper polariton (UP) and the low-energy lower polariton (LP). Here, $\hbar$ is the reduced Planck constant; ω_{ex} and ω_{ph} denote the exciton and photon resonance frequencies, respectively; $|X\rangle$ represents the bare exciton state; and $|Cav\rangle$ represents the bare cavity photon state.

nature of which can be revealed by the wave function properties: the polariton wave function can be described as a linear superposition of photon and matter excitations[48,49]. This particular quantum superposition state determines the way energy is distributed in the light-matter system and the energy transport process. Specifically, the exciton-polariton state causes oscillations between photons and excitons at the Rabi frequency, i.e., photons are periodically absorbed and re-emitted through the exciton state. Under strong coupling conditions, the effective mass, and therefore the transport, is mainly determined by the photon composition, and the excitons are able to achieve transport through photonic modes, so that exciton transport can be improved to exhibit longer diffusion lengths. The hypothesized principle of photocurrent generation is similar to that of pure exciton photovoltaic devices, i.e., the exciton dissociates into a free charge at the interface, but in strong coupling, the exciton is transported in a photon-like mode and dissociates at the charge-selective contact, one charge being immediately extracted while the opposite free charge undergoes drift-diffusion transport to the other contact. In this study, we leverage the strong absorption and low effective mass of EPs to enhance the performance of photodiodes. In Fig. 1d, we schematically elucidate the relationship between the emergence of multiple polariton branches in the WS_2 strong coupling device. The exciton-polariton states can enhance the subgap photon absorption and exciton diffusion length, which can minimize the energy loss and improve the quantum efficiency. While the presence of polaritons in our devices is clearly evidenced by enhanced absorption and spectral quantum efficiency, the overall photodetector performance, particularly the response speed, remains below the theoretical polaritonic limits owing to material and interface imperfections. Interfacial trap states induce nonradiative recombination and hinder carrier extraction, while non-ideal contact geometry may further constrain carrier collection dynamics. Importantly, these are technological rather than fundamental limitations. Advancing crystal and interface quality (e.g., through improved encapsulation and transfer processes), optimizing dielectric environments, and especially implementing carefully designed integrated cavities with higher Q factors and tighter mode confinement could substantially enhance the light-matter coupling strength and absorption efficiency. Together with refined electrode configurations for rapid carrier extraction, these improvements could bridge the gap toward the theoretical performance limits of polaritonic photodetectors.

Strong coupling in self-hybridized polaritonic photodiodes

We performed thickness-dependent reflectance measurements, transfer matrix method (TMM) calculations, and fitting to the coupled oscillator model to confirm the presence of strong coupling in our devices[50]. Figure 2a shows the TMM-calculated thickness and wavelength-dependent reflectance of our devices. Polaritons appear in the calculated reflectance spectra as reflectance minima that exhibit anti-crossing behavior near the exciton resonance (approximately 1.97 eV for WS_2, denoted by the yellow vertical dotted lines in Fig. 2a, b). For each cavity mode order, the dispersion is fit with the coupled oscillator model, in which we include decay of the exciton and cavity modes[22,51]. The resulting fit is overlaid in Fig. 2a as dashed white lines, and the corresponding bare cavity modes are overlaid as red dashed lines. The Rabi splitting values between the upper and lower polariton branches (UPB and LPB) for the first 3 FP cavity modes ($l = 1,2,3$) are found to be $\hbar\Omega = 152.62$ meV ($l = 1$), 173.38 meV ($l = 2$), and 171.42 meV ($l = 3$), respectively (Supplementary Fig. 3). The real values of Rabi splitting confirm that the devices are in the strong coupling regime when thicknesses support cavity modes with resonances near the A exciton. For thicknesses below approximately 50 nm, the devices are in the weak coupling regime, as evidenced by the asymmetric Fano resonance slightly blue shifted from the exciton resonance[52].

Figure 2b shows experimentally measured and reflectance spectra for representative devices of varying thickness. The corresponding TMM calculations (dashed black lines) match the measured spectra very well. The dispersion of the UPB and LPB is shown by the purple dotted lines. Spectra are offset vertically for clarity. Notably, the absorbance is large and broadband, and the polariton branches can be seen to extend the spectral range of absorption while exhibiting near unity absorption. To further resolve weak or overlapping features, we performed derivative analysis of the measured spectra (Supplementary Fig. 5)[53]. The first derivatives (Supplementary Fig. 5b) highlight inflection points corresponding to reflectance extrema, revealing subtle spectral features otherwise obscured in the raw data. Representative derivative spectra (Supplementary Fig. 5c) for devices in the strong-coupling regime (151.2 nm, 77.3 nm) display two well-resolved peaks straddling the A-exciton energy, fully consistent with the formation of UPB and LPB. Angle-resolved reflectivity spectra of devices with different thicknesses further reveal the coupling regime. Pronounced anti-crossing features were observed for WS_2 layers thicker than 50 nm, consistent with strong exciton-photon hybridization, while thinner devices displayed only a dispersionless excitonic resonance. Coupled oscillator model fits quantitatively reproduce the experimental dispersions and confirm strong coupling across representative thicknesses (see Supplementary Fig. 6, Table 1). More detailed information on the simulation method is provided in the Supplementary Fig. 3 section.

EQE spectra driven by exciton-polariton states

We now consider the spectral response of WS_2 photodiodes operating in the strong coupling regime. EQE is an important metric for photodiodes and photovoltaics as it reflects the ratio of the charge carrier flux (i.e., current density) collected at the electrodes to the incident photon flux at a specific excitation wavelength. EQE measurements ("methods") are performed in the 500 nm to 800 nm range on devices with WS_2 thicknesses from 17 to 200 nm (Supplementary Fig. 9). To accurately identify the polariton-related photocurrent features, we performed first-derivative analysis of the EQE spectra (Supplementary Fig. 9b, c). This method sharpens spectral features and pinpoints inflection points that correspond to EQE maxima. Figure 2c shows the coupled oscillator model fit, along with the experimental EQE peak wavelengths extracted from a range of device thicknesses (Supplementary Fig. 9b). Notably, the peak response positions of the EQE spectra in devices with varying thicknesses (scattered dots) exhibit excellent agreement with the theoretical model (dashed lines). In particular, the evolution of their wavelength positions with thickness strictly follows the characteristic dispersion relation of polaritons, with the peak positions corresponding to the resonance modes of the UP and LP branches, respectively. This consistency between experimental observations and the theoretical model provides solid evidence that the polariton state enhances light-trapping efficiency by modulating photon-exciton interactions, clearly demonstrating the crucial role of polariton engineering in improving photodiode performance. Figure 2d shows the EQE spectra of three representative devices, one in the weak coupling regime, one near zero detuning for the first-order polariton, and one near zero detuning for the second-order polariton. In these strongly coupled devices, both the UPB and LPB exhibit spectral separations from the bare exciton resonance that exceed their respective linewidths. This clear spectral separation enables unambiguous identification of the polariton branches. The responses below the bare exciton energy of the strongly coupled devices can be observed, and the peaks of the responses correspond to the reflectance minima (attributed to UP and LP branches) reported in the previous section (Fig. 2b). These features are absent in weakly coupled devices, confirming that all these responses are dominated by the exciton-polariton states. Based on this, we can predict that the strong-

https://doi.org/10.1038/s41467-026-68312-8

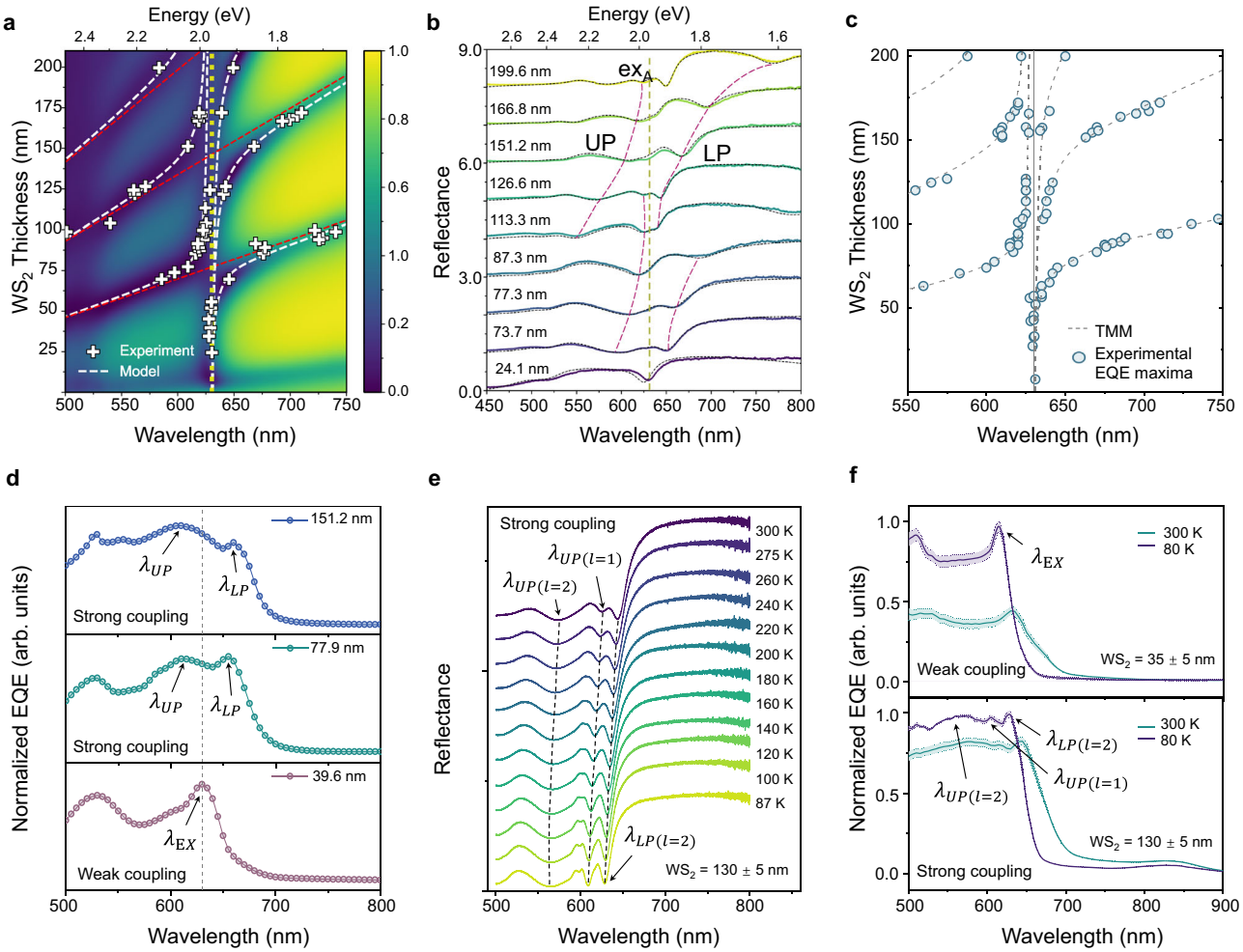

Fig. 2 | Exciton-polariton dispersion and thickness-dependent External Quantum Efficiency (EQE) of multi-layer WS_2 devices in strong coupling. **a** Thickness- and wavelength-dependent reflectance calculated using the transfer matrix method (TMM), showing the dispersion of the exciton polaritons. The white dashed lines show the coupled-oscillator fit to the calculated reflectance minima, representing the polariton dispersion. The bare cavity mode dispersion (red dashed lines) and the exciton wavelength λ_{EX} corresponding to the A-exciton energy (yellow dotted lines) are overlaid. The white cross-hairs indicate experimentally measured reflectance minima. The indices $l = 1, 2$ denote the Fabry-Pérot cavity mode orders. **b** Experimental reflectance spectra of WS_2 devices with varying WS_2 thickness. The upper and lower polariton branches (UPB and LPB) are highlighted with purple dashed lines. The black dashed lines show the corresponding reflectance spectra calculated by TMM. The yellow vertical dashed line marks the wavelength corresponding to the A-exciton energy. **c** Dots are extracted from experimental EQE spectra shown in (Supplementary Fig. 9), while lines are the calculated dispersions of the polariton eigenstates. The EQE experimental data agree well with the calculated polariton branches of the coupled oscillator model. **d** Self-normalized EQE spectra for WS_2 thicknesses of 151.2 nm, 77.9 nm, and 39.6 nm. Both devices in the strong coupling regime (151.2 nm, 77.9 nm) show two EQE peaks on either side of the ex_A energy corresponding to the well-defined upper (λ_{UP}) and lower (λ_{LP}) polariton branches. **e** Temperature-dependent reflectance spectra of devices in strong coupling regimes. The polaritonic branches remain clearly resolved across the entire temperature range without merging into a single resonance, confirming the persistence of strong coupling. **f** Corresponding relative external quantum efficiency (EQE) response spectra for weakly and strongly coupled devices at 300 K and 80 K. The error bands represent the experimental value variation (standard deviation).

coupling device can harvest more photons in the spectral region around the bandgap due to the formation of exciton-polariton states.

Further, we note that the response of the photodiodes is broadband, highlighting the benefit of the ITO ARC. Simultaneously, the cut-off wavelength of the device is extended (Supplementary Fig. 11). Compared with conventional excitonic materials, the narrow-band absorption properties due to the strong exciton binding effect and the ability to achieve high absorption efficiency only at specific wavelengths are avoided.

In addition, to further explore whether the exciton properties are preserved during the transport process and the effect of polariton coupling on quantum efficiency, we performed reflectance spectra, I–V characteristics, and EQE spectra measurements at low temperatures (Fig. 2e, f, Supplementary Figs. 12, 13). The results show that:

i) A comparison of the I-V curves at 300 K and 80 K reveals a significant reduction in dark current, attributed to the decreased concentration of thermally excited carriers, indicating a lower density of free carriers at low temperatures.

ii) In both strong- and weak-coupling devices, we observe a pronounced steepening of the exciton absorption edges, a blue shift of the absorption maxima, and an enhancement of the EQE at low temperatures under both resonant and non-resonant excitation, reflecting the strengthened excitonic and polaritonic effects. Such enhancement may also partially arise from polariton-mediated modification of radiative rates (Purcell-like effect)[54], suggesting a direction for future studies to quantitatively evaluate this effect. Correspondingly, the absorption peaks dominated by the UPB and LPB are also clearly resolved in the EQE spectra, as indicated by the black arrows in Fig.2f. To capture the full thermal evolution of these coupled states, we

https://doi.org/10.1038/s41467-026-68312-8

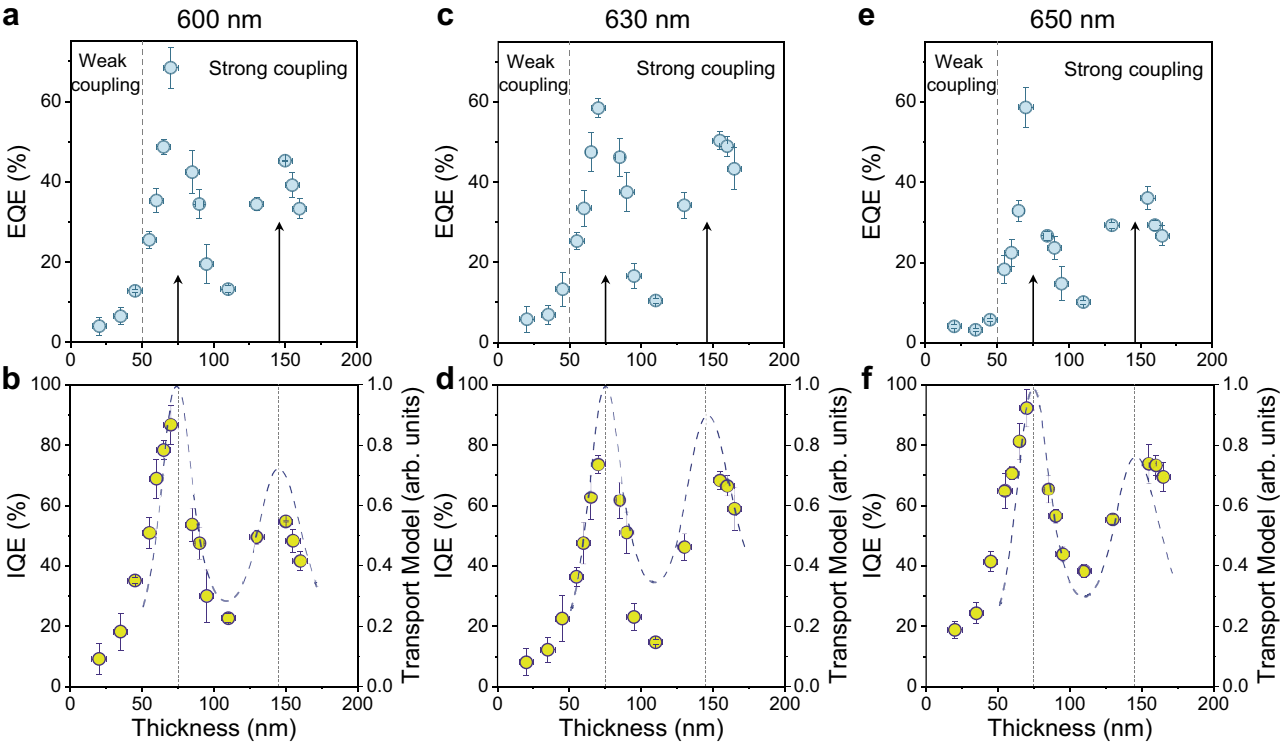

Fig. 3 | Thickness varying quantum efficiency in polaritonic photodiodes. EQE and internal quantum efficiency(IQE) variation of the multilayer WS_2 photodiode devices with different thicknesses at 600 nm (**a**, **b**), 630 nm (**c**, **d**), and 650 nm (**e**, **f**). The thicknesses of WS_2, approximately 75 nm and 145 nm, corresponding to the zero detuning of the l = 1,2 cavity mode, are marked by gray lines. The error bar represents the variation of experimental values (standard deviation).

carried out continuous temperature-dependent reflectance spectra from 87 K to 300 K on WS_2 cavities with thicknesses ranging from ~35 nm to ~130 nm. Across all devices, the UPB and LPB display a smooth, monotonic redshift with increasing temperature. Importantly, the polariton branches remain spectrally resolved over the entire temperature range without collapsing into a single peak, confirming that the system persistently resides in the strong-coupling regime. The temperature-induced evolution of the spectral splitting is accompanied by consistent trends in the EQE spectra, with devices near zero detuning exhibiting distinct peak splitting even at elevated temperatures. These observations substantiate the assignment of the observed features to robust exciton-photon hybrid states (polaritons), rather than to uncoupled optical modes or interference fringes.

Based on these observations, we speculate that at low temperatures, the EQE is predominantly dominated by exciton and polariton contributions, owing to the preservation and enhancement of exciton and polariton properties of WS_2 and the suppression of the free-carrier effect. This further demonstrates that polaritons contribute to photovoltaic conversion and could potentially be exploited to enhance exciton transport and improve the photonic energy conversion efficiency of excitonic semiconductors.

External and internal quantum efficiency

To quantify the effect of strong coupling on the overall photoelectric conversion efficiency and the internal processes of the WS_2 devices, we calculated the EQE and the IQE of the devices as a function of thickness for wavelengths of 600 nm, 630 nm, and 650 nm (Fig. 3). To eliminate uncertainty, at each thickness, we prepared multiple devices with similar thicknesses (≥3) and performed multiple measurements (≥5), then extracted the mean and standard deviation. The EQE reflects both the absorption and internal excitation-to-charge collection processes in the device. It is known that polaritons enhance absorption on resonance and can extend the spectral responsivity of photodiodes through absorption in the LPB. Polaritons are also expected to improve carrier extraction due to improved exciton diffusion. The greatest hybridization (i.e. strongest coupling) between photons and excitons occurs when there is zero detuning between the photonic mode and the exciton energy. In our devices, this occurs at WS_2 thicknesses of approximately 75 nm for the first FP cavity mode and 145 nm for the second FP cavity mode. Consequently, we see oscillatory behavior in the EQE with thickness, with peaks near the first and second zero detuning thicknesses, evidencing the beneficial effects of strong coupling. In addition to the oscillatory behavior, there is a drastic increase in EQE for all wavelengths as the thickness enters the strong coupling regime. The increase in EQE from the weak coupling regime to the strong coupling regime is a factor of about 20 near the polariton resonance (600 nm,650 nm) and a factor of about 10 at the exciton wavelength (630 nm).

We now consider the IQE to determine the degree to which strong-coupling affects exciton transport and carrier extraction. Owing to the enhanced electric fields associated with polariton states, the electrode layers display parasitic absorption peaks (Supplementary Fig. 10). The IQE only reflects the charge collection process for photons absorbed in the WS_2 active layer. IQE is calculated as the quotient of EQE and the percentage of photons absorbed in the separate WS_2 layer under short-circuit conditions, and the percentage of photons dissipated in the separate WS_2 layer can be extracted from layer-resolved absorption with the transfer matrix model (Supplementary Fig. 10). IQE decreases with increasing active layer thickness in conventional photovoltaic devices[55–58]. However, the IQE data in Fig. 3 show a strong oscillatory behavior with increasing WS_2 thickness. For thin layers, both IQE and EQE exhibit lower values, partly due to (i) the limited light absorption of the thin material under weak coupling, (ii) more effects of interfacial defect recombination for thinner absorber layers, and (iii) contact-induced variability. Notably, A large increase in the IQE is observed as the thickness increases into the strong coupling

regime, with a strong peak at the zero-detuning thickness for the first-order polariton. Near unity IQE is achieved for on-resonance devices. This enhancement arises from self-hybridized polariton states that concentrate optical fields within the WS_2 layer, enabled by the device geometry used here.

We include in the IQE plots for Fig. 3 a phenomenological transport model (dashed line) to predict the effect of strong coupling enhanced transport as a function of WS_2 thickness. Our model assumes a hopping-based exciton diffusion process in which a random walk occurs through a resonance energy transport (RET) mechanism[14,59–61]. Here, we expect that homogeneous RET occurs between identical but spatially separated molecules through the electric field associated with polariton states[61]. This concept is consistent with both the quantum electrodynamics formulation of RET and the concept of EPs[62], in which the dipole-dipole interactions between light and matter can be interpreted as the rapid emission and reabsorption of cavity photons through excitons[18]. The resulting RET-based diffusivity is weighted by the thickness-dependent exciton fraction of the polariton branch and then multiplied by an exponentially decaying envelope function to represent free carriers having a greater chance of recombining in the bulk as thickness increases. This model is then fit to experimental data and represented as a phenomenological transport model in arbitrary units. We can use this model to qualitatively analyze the oscillatory trend of IQE-related diffusion coefficients at specific wavelengths and at which thicknesses the peaks are located. For more discussion of the transport model, please refer to the Supplementary Information (Supplementary Fig. 14). Figure 3b shows that the fitting results of the phenomenological model are in agreement with the trend of the experimental data, suggesting that the enhancement of the IQE is mainly due to improved exciton transport in the strong coupling regime.

Photovoltaic detection of polaritonic photodiodes

Finally, we evaluated the comprehensive detection performance of the exciton-polariton photodiode. Figure 4a shows the dark and optical current density curves for a representative device. The dark current density is as low as 5.33×10^{-7} A cm^{-2} at 0 V, indicating relatively low noise current and high sensitivity. Simultaneously, a light-switching ratio (I_{on}/I_{off} ratio) of 7.1×10^5 is obtained. Compared with other exciton photodetectors, our photodiode exhibits lower dark current density and higher I_{on}/I_{off} ratio (Supplementary Table 1). Fig. S15 (Supporting Information) presents the photocurrent versus light power for three representative devices operated in strong and weak coupling under 600 nm, 630 nm, and 650 nm illumination. The dependence of the photocurrent on the light intensity is fitted to a power law equation ($y = bx^{\alpha}$) from which $\alpha = 1.01$ to 1.04 is obtained. This confirms that the device has a good linear photovoltaic response, indicating high efficiency, as all the excited electrons/holes are captured by the electrodes before recombination[63].

The responsivity (R) is closely related to strong coupling due to the benefits of increased absorption and polaritonic transport. Consequently, the trend observed in EQE should be mirrored in R. We calculated the variation of R with thickness for devices at wavelengths of 600 nm, 630 nm, and 650 nm when V = 0 V is applied (Fig. 4b, Supplementary Fig. 16). This effect is confirmed by oscillatory behavior, with a significant increase in responsivity corresponding to polariton-induced transport. The maximum responsivity obtained is 0.35 A/W (600 nm, 15 µW), located near the first zero-detuned thicknesses. Additionally, there is a strong initial increase in responsivity as the strong coupling state is entered.

Noise equivalent power (*NEP*) is a key parameter for evaluating the ability of a photodetector to detect weak radiation and is defined as $NEP = i_n/R$ (i_n is the dark current noise). Typically, dark current noise is caused by shot noise, thermal noise, and 1/f noise[64]. To fully account for frequency-dependent noise, the current noise power spectra of the device are measured at zero bias using a signal analyzer and a low-noise preamplifier (Supplementary Fig. 17). From the directly measured noise, we calculated ${i_n}^2$ using the equation ${i_n}^2 = \frac{1}{B}\int_0^B S_n(f)df$ where B is the bandwidth. Then we calculated the *NEP* at 0 V bias as shown in Fig. 4c. The *NEP* value is obtained to be 0.34 pw Hz$^{-1/2}$ at $WS_2 = 73.5$ nm under 630 nm illumination. The lower *NEP* indicates that the device has an excellent capability to distinguish between signal and noise, which can be achieved at high photoresponsivity and low current-noise power density.

Fast photoresponse is a key performance metric for photodetectors. We anticipate that the speed of the photodiode can be increased by utilizing enhanced transport through photonic modes. Therefore, we measured the response speed at a frequency of 10 kHz with a 520 nm laser at 0 V bias. As shown in Fig. 4d, we extracted the rise time as a function of WS_2 thickness. The increase of the response speed in the strong-coupling state and the obvious peak at zero detuning thickness confirm the expected behavior. The fastest response in the strong coupling state is about 217 ns ($WS_2 = 73.5$ nm). Supplementary Fig. 18 and Fig. 19 (Supporting Information) show numerous measurements of the response speed of a representative device in the strong- and weak-coupling states as well as typical response time curves, further confirming our conclusions. In addition, we obtained a −3 dB cut-off frequency of 1.21 MHz ($WS_2 = 73.5$ nm), which is extracted from the frequency-dependent photoresponse of the signal at a 520 nm laser at the modulation frequency as it drops to 70.7% of its initial value, as shown in Fig. 4e. The rise time τ_r can be estimated as 289.2 ns using the equation $\tau_r = 0.35/f_{-3dB}$, which is similar to the response time measurement. Generally, the intrinsic lifetimes of excitons and polaritons fall within the picosecond-sub-nanosecond range, and the nanosecond-scale device photoresponse observed here was influenced by interfacial carrier trapping (Supplementary Fig. 20), suggesting that further suppression of interfacial defects can enable even faster operation. To further verify the performance enhancement of the polariton photodiode, we compared our device with other structures. Figure 4f shows the room temperature responsivity and response speed compared to other excitonic photodetectors. Our photodetectors both exhibit response times of several hundred nanoseconds at room temperature, which is faster than most excitonic photodetectors, as shown in Supplementary Table 3. Therefore, we can conclude that self-hybridized exciton polariton photodiodes are extremely attractive for high-efficiency, fast photodetection.

Discussion

In conclusion, we demonstrate polaritonic photodiodes with self-hybridization of light and matter in WS_2. These photodiodes show broadband absorption and polariton-enhanced transport for improved quantum efficiency approaching unity near the zero detuning condition and oscillating with thickness-dependent resonance, in agreement with phenomenological theory as well as electromagnetic simulations. Given that excitonic transport limited by diffusion length is the primary reason for limited efficiencies in many excitonic semiconductor-based photodetector devices, our result of using polaritons to enhance diffusion represents a potential breakthrough. In addition, our optical design shows broadband absorption and innovative use of transparent conducting electrodes as top contacts and anti-reflective layers concurrently for ultrathin photodiodes. The simultaneous presence of broadband absorption and strong coupling-enhanced exciton transport makes open cavity, self-hybridized exciton polariton devices highly attractive for detectors. The use of strongly-coupled light and matter in the form of exciton-

https://doi.org/10.1038/s41467-026-68312-8

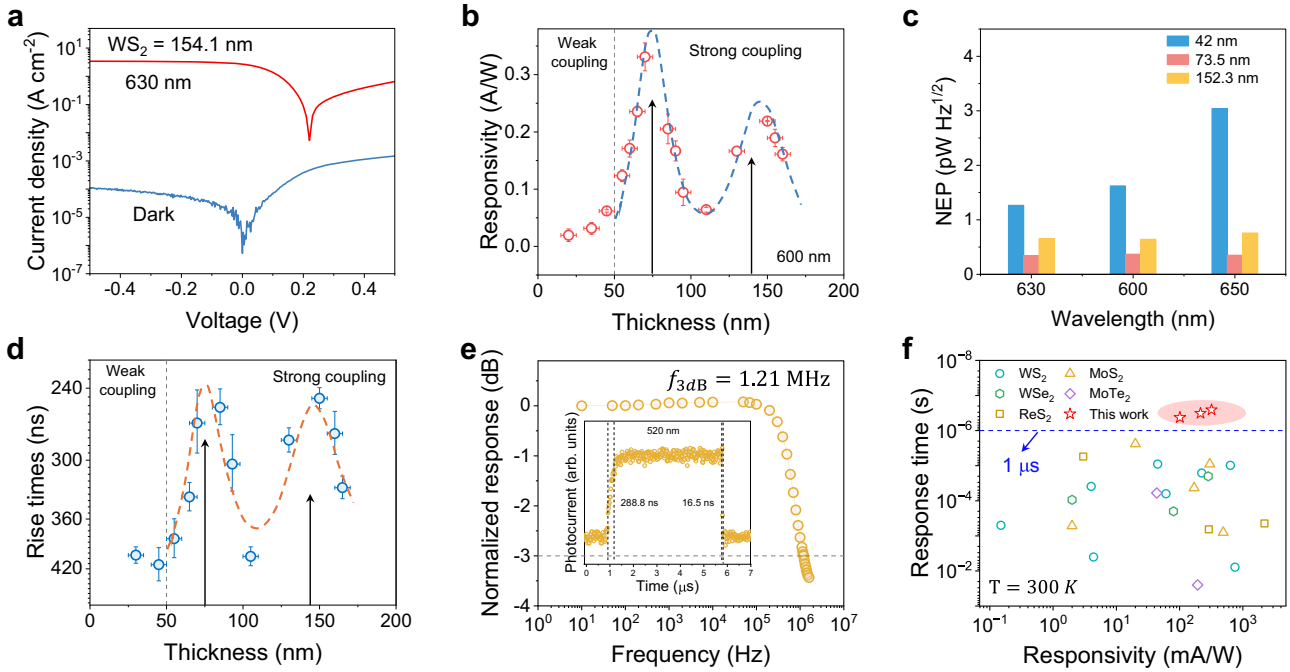

Fig. 4 | Photovoltaic detection performance of Polaritonic photodiodes at room temperature. a Photocurrent density and dark current density curves for a champion device. **b** Responsivity as a function of thickness. The error bar represents the variation of experimental values (standard deviation). (600 nm,15 μW) **c** Noise equivalent power (*NEP*) for WS_2 thicknesses of 152.3 nm, 73.5 nm, and 42 nm. **d** Response time as a function of thickness. The error bar represents the variation of experimental values (standard deviation). **e** Normalized photoresponse with the modulation frequency measured for a strong device (WS_2 = 73.5 nm). Inset: The time-dependent current of the device. f_{-3dB} denotes the −3 dB cut-off frequency, defined as the frequency at which the photoresponse drops to 70.7% of its initial value. **f** Comparison of responsivity and response time among previous reports. References to the selected work can be found in Supplementary Table 1.

polaritons in absorptive optoelectronic devices represents a paradigm shift in the physics and device design of all such systems based on excitonic semiconductors.

Methods

Device fabrication

The bottom electrical contacts are patterned using electron-beam lithography and then electron-beam evaporation deposition of 3 nm Cr and 100 nm Au on a silicon substrate with 300 nm SiO_2 (University Wafer). WS_2 layers are mechanically exfoliated from bulk crystals (HQ Graphene) with blue adhesive film tape and transferred onto the surface of a polydimethylsiloxane stamp. WS_2 layers are transferred by an all-dry deterministic transfer procedure on the preprepared bottom electrical contacts by using a polydimethylsiloxane stamp. The top electrical contacts are patterned with electron beam lithography and ion beam sputtering deposition of 50 nm ITO. All devices after fabrication were annealed in an N_2 environment. The resulting devices are identified by optical microscopy and later characterized by atomic force microscopy (AFM, Asylum Research MFP−3D Origin) to determine the flake thickness.

Reflectance measurements

The WS_2 device reflectance spectra were measured using a home-built micro-reflection system (see Supplementary Fig. 21) with a 50× objective (Olympus, NA = 0.45) under normal incidence. Dispersion relations in reflection were measured using a 100× objective (NA = 0.9). The illumination source used in the measurements is 10–250 W tunable Quartz Tungsten Halogen lamps (Newport 66884 Research QTH Lamp), and the reflectance signals were gathered by a grating spectrometer equipped with a CCD (SpectraPro HRS-500). The reflectance spectra are normalized by the reflectance of a silver mirror (Thorlabs).

Determination of optical constants

The optical constants of ITO, Au used in our simulations are obtained by spectroscopic ellipsometry (Supplementary Fig. 2). The optical constants of WS_2 are assumed to be thickness-independent bulk optical constants of WS_2 from literature[65]. This is due to the fact that the phenomena reported in this study are concentrated in the 17–200 nm thickness range, which represents the electron bulk in WS_2, as the effect of electron quantum confinement becomes negligible at about 5 nm (6–7 layers) thickness[40].

Electrical and optoelectronic measurements

The light of a supercontinuum white light laser (Fianium WhiteLase SC400) is coupled into a tunable, high-resolution bandpass filter (LLTF Contrast SR-VIS-HP8). The resulting monochromatic beam was focused onto the WS_2 device through a fixed optical path using a 20× objective lens (NA = 0.45), producing a spot with a diameter of approximately 12 μm. Under short-circuit conditions, the photocurrent was amplified by a low-noise current preamplifier (Stanford Research Systems SR570) and subsequently analyzed using a lock-in amplifier (Stanford Research Systems SR865A) (shown in Supplementary Fig. 22). The EQE is determined by dividing the photocurrent of the WS_2 device by the flux of incoming photons, which is obtained with calibrated silicon (Si) and indium–gallium–arsenide (InGaAs) photodiodes. For photocurrent mapping measurements, the laser beam was focused onto the device through a fixed optical path using a 50× objective lens (NA = 0.6), yielding a laser spot diameter of approximately ~2 μm. The data on response time were acquired using a Tektronix MDO34 oscilloscope. The noise current spectrum was measured by using a preamplifier (DL1211) and a signal analyzer (Keysight N9010B) in a shielding box. The electronic characteristics were measured by a Keysight B2912A source. For low temperature measurements (up to 80 K), the samples were placed in a cryostat and cooled

down to the desired temperature by controlling the flow of liquid nitrogen.

Data availability

The Source data underlying the figures of this study are available with the paper and are accessible at https://figshare.com/s/7a581a95641b550b759c. All raw data generated during the current study are available from the corresponding authors upon request. Source data are provided with this paper.

Code availability

The codes used for simulation and data plotting are available from the corresponding authors upon request.

References

1. Lukman, S. et al. High oscillator strength interlayer excitons in two-dimensional heterostructures for mid-infrared photodetection. *Nat. Nanotechnol.* **15**, 675–682 (2020).
2. Chen, P. et al. Approaching the Intrinsic exciton physics limit in two-dimensional semiconductor diodes. *Nature* **599**, 404–410 (2021).
3. Hong, E., Li, Z., Zhang, X. & Fang, X. Light-state rectification behaviors induced by interlayer excitons in mixed-dimensional single-crystalline perovskite heterostructures. *Adv. Funct. Mater.* **35**, 2412189 (2025).
4. Jang, Y. J. et al. Boosting internal quantum efficiency via ultrafast triplet transfer to 2H-$MoTe_2$ film. *Sci. Adv.* **9**, g2324 (2023).
5. Park, S. Y. et al. Photophysical pathways in efficient bilayer organic solar cells: the importance of interlayer energy transfer. *Nano Energy* **84**, 105924 (2021).
6. Hu, Z., Lin, D., Lynch, J., Xu, K. & Jariwala, D. How good can 2D excitonic solar cells be?. *Device* **1**, 100003 (2023).
7. Jariwala, D., Davoyan, A. R., Wong, J. & Atwater, H. A. Van Der Waals materials for atomically-thin photovoltaics: promise and outlook. *ACS Photonics* **4**, 2962–2970 (2017).
8. Ma, Y. et al. Breaking the size limit of room-temperature prepared lead sulfide colloidal quantum dots for high-performance short-wave infrared optoelectronics. *ACS Photonics* **12**, 1116–1124 (2025).
9. Sheehan, T. J., Saris, S. & Tisdale, W. A. Exciton transport in perovskite materials. *Adv. Mater.* **37**, 2415757 (2024).
10. Bernardi, M., Palummo, M. & Grossman, J. C. Extraordinary sunlight absorption and one-nanometer-thickness photovoltaics using two-dimensional monolayer materials. *Nano Lett.* **13**, 3664–3670 (2013).
11. Chernikov, A. et al. Measurement of the optical dielectric function of monolayer transition-metal dichalcogenides: MoS_2, $MoSe_2$, WS_2, and WSe_2. *Phys. Rev. B* **90**, 205422 (2014).
12. Went, C. M. et al. A new metal transfer process for van der waals contacts to vertical schottky-junction transition metal dichalcogenide photovoltaics. *Sci. Adv.* **5**, x6061 (2019).
13. Mikhnenko, O. V., Blom, P. W. M. & Nguyen, T. Exciton diffusion in organic semiconductors. *Energy Environ. Sci.* **8**, 1867–1888 (2015).
14. Menke, S. M. & Holmes, R. J. Exciton diffusion in organic photovoltaic cells. *Energy Environ. Sci.* **7**, 499–512 (2014).
15. Paul, K. K., Kim, J. & Lee, Y. H. Hot carrier photovoltaics in Van Der Waals heterostructures. *Nat. Rev. Phys.* **3**, 178–192 (2021).
16. Anantharaman, S. B., Jo, K. & Jariwala, D. Exciton–photonics: from fundamental science to applications. *ACS Nano* **15**, 12628–12654 (2021).
17. Zhao, L. et al. Strong exciton-photon interaction and lasing of two-dimensional transition metal dichalcogenide semiconductors. *Nano Res.* **14**, 1937–1954 (2021).
18. Gibbs, H. M., Khitrova, G. & Koch, S. W. Exciton–polariton light–semiconductor coupling effects. *Nat. Photonics* **5**, 273 (2011).
19. Su, R. et al. Perovskite semiconductors for room-temperature exciton-polaritonics. *Nat. Mater.* **20**, 1315–1324 (2021).
20. Song, J. et al. Room-temperature continuous-wave pumped exciton polariton condensation in a perovskite microcavity. *Sci. Adv.* **11**, r1652 (2025).
21. Alfieri, A. D., Ruth, T., Lim, C., Lynch, J. & Jariwala, D. Effects of self-hybridized exciton-polaritons on Tmdc photovoltaics. *Nano Lett.* **25**, 3020–3026 (2025).
22. Sanvitto, D. & Kéna-Cohen, S. The road towards polaritonic devices. *Nat. Mater.* **15**, 1061–1073 (2016).
23. Liu, G. et al. Long-range ballistic motion and coherent flow of long-lifetime polaritons. *Phys. Rev. B* **88**, 235314 (2013).
24. Liu, B. et al. Long-range propagation of exciton-polaritons in large-area 2D semiconductor monolayers. *ACS Nano* **17**, 14442–14448 (2023).
25. Zhong, X. et al. Non-radiative energy transfer mediated by hybrid light-matter states. *Angew. Chem. Int. Ed.* **55**, 6202–6206 (2016).
26. Son, M. Energy cascades in donor-acceptor exciton-polaritons observed by ultrafast two-dimensional white-light spectroscopy. *Nat. Commun.* **13**, 7305 (2022).
27. Xu, D. et al. Ultrafast imaging of polariton propagation and interactions. *Nat. Commun.* **14**, 3881 (2023).
28. Nikolis, V. C. et al. Strong light-matter coupling for reduced photon energy losses in organic photovoltaics. *Nat. Commun.* **10**, 1–8 (2019).
29. Wang, M., Hertzog, M. & Börjesson, K. Polariton-assisted excitation energy channeling in organic heterojunctions. *Nat. Commun.* **12**, 1874 (2021).
30. Liu, B., Huang, X., Hou, S., Fan, D. & Forrest, S. R. Photocurrent generation following long-range propagation of organic exciton-polaritons. *Optica* **9**, 1029 (2022).
31. Eizner, E., Brodeur, J., Barachati, F., Sridharan, A. & Kéna-Cohen, S. Organic photodiodes with an extended responsivity using ultrastrong light–matter coupling. *ACS Photonics* **5**, 2921–2927 (2018).
32. de Jong, L. M. A. et al. Enhancement of the internal quantum efficiency in strongly coupled P3Ht-C_{60} organic photovoltaic cells using fabry–perot cavities with varied cavity confinement. *Nanophotonics* **13**, 2531–2540 (2024).
33. Tang, Y., Stuart, A. N., van der Laan, T. & Lakhwani, G. Strong light–matter coupling leads to a longer charge carrier lifetime in cavity organic solar cells. *ACS Photonics* **11**, 1627–1637 (2024).
34. Pandya, R. et al. Microcavity-like exciton-polaritons can be the primary photoexcitation in bare organic semiconductors. *Nat. Commun.* **12**, 6519 (2021).
35. Anantharaman, S. B. et al. Dynamics of self-hybridized exciton-polaritons in 2D halide perovskites. *Light Sci. Appl.* **13**, 1 (2024).
36. Yuan, L., Wang, T., Zhu, T., Zhou, M. & Huang, L. Exciton dynamics, transport, and annihilation in atomically thin two-dimensional semiconductors. *J. Phys. Chem. Lett.* **8**, 3371–3379 (2017).
37. Jariwala, D. et al. Near-unity absorption in Van Der Waals semiconductors for ultrathin optoelectronics. *Nano Lett.* **16**, 5482–5487 (2016).
38. Liu, X. et al. Strong light–matter coupling in two-dimensional atomic crystals. *Nat. Photonics* **9**, 30–34 (2015).
39. Alfieri, A. D. et al. Ultrathin broadband metasurface superabsorbers from a Van Der Waals semimetal. *Adv. Opt. Mater.* **11**, 2202011 (2023).
40. Zhang, H. et al. Hybrid exciton-plasmon-polaritons in Van Der Waals semiconductor gratings. *Nat. Commun.* **11**, 3552 (2020).
41. Munkhbat, B. et al. Self-hybridized exciton-polaritons in multilayers of transition metal dichalcogenides for efficient light absorption. *ACS Photonics* **6**, 139–147 (2019).
42. Barachati, F. et al. Interacting polariton fluids in a monolayer of tungsten disulfide. *Nat. Nanotechnol.* **13**, 906–909 (2018).
43. Sermage, B., Tiberj, A., Planel, R. & Freixanet, T. In-plane propagation of excitonic cavity polaritons. *Phys. Rev. B* **61**, 7233–7236 (2000).

44. Shi, Y. et al. Coherent optical spin hall transport for polaritonics at room temperature. *Nat. Mater.* **24**, 56–62 (2025).
45. Balasubrahmaniyam, M. et al. From enhanced diffusion to ultrafast ballistic motion of hybrid light–matter excitations. *Nat. Mater.* **22**, 338–344 (2023).
46. Tichauer, R. H., Sokolovskii, I. & Groenhof, G. Tuning the coherent propagation of organic exciton-polaritons through the cavity Q-factor. *Adv. Sci.* **10**, 2302650 (2023).
47. Orgiu, E. et al. Conductivity in organic semiconductors hybridized with the vacuum field. *Nat. Mater.* **14**, 1123–1129 (2015).
48. Quattropani, A., Andreani, L. C. & Bassani, F. Quantum theory of polaritons with spatial dispersion: exact solutions. *Il Nuovo Cimento D* **7**, 55–69 (1986).
49. Kasprzak, J. et al. Bose–einstein condensation of exciton polaritons. *Nature* **443**, 409–414 (2006).
50. Pettersson, L. A. A., Roman, L. S. & Inganäs, O. Modeling photocurrent action spectra of photovoltaic devices based on organic thin films. *J. Appl. Phys.* **86**, 487–496 (1999).
51. Georgiou, K., Jayaprakash, R., Othonos, A. & Lidzey, D. G. Ultralong-range polariton-assisted energy transfer in organic microcavities. *Angew. Chem. Int. Ed.* **60**, 16661–16667 (2021).
52. Limonov, M. F., Rybin, M. V., Poddubny, A. N. & Kivshar, Y. S. Fano resonances in photonics. *Nat. Photonics* **11**, 543–554 (2017).
53. Berkelbach, T. C. et al. Exciton binding energy and nonhydrogenic rydberg series in monolayer WS_2. *Phys. Rev. Lett.* **113**, 76802 (2014).
54. Zhao, H., Arneson, C. E., Fan, D. & Forrest, S. R. Stable blue phosphorescent organic leds that use polariton-enhanced purcell effects. *Nature* **626**, 300–305 (2024).
55. Park, H. et al. Thickness-dependent internal quantum efficiency of narrow band-gap polymer-based solar cells. *Sol. Energy Mater. Sol. Cells* **143**, 242–249 (2015).
56. Hädrich, M., Metzner, H., Reislöhner, U. & Kraft, C. Modelling the quantum efficiency of cadmium telluride solar cells. *Sol. Energy Mater. Sol. Cells* **95**, 887–893 (2011).
57. Law, M. et al. Determining the internal quantum efficiency of pbse nanocrystal solar cells with the aid of an optical model. *Nano Lett.* **8**, 3904–3910 (2008).
58. Scheunemann, D., Wilken, S., Parisi, J. & Borchert, H. Investigation of the spatially dependent charge collection probability in $CuInS_2$/ZnO colloidal nanocrystal solar cells. *ACS Photonics* **2**, 864–875 (2015).
59. Zhong, X. et al. Energy transfer between spatially separated entangled molecules. *Angew. Chem. Int. Ed.* **56**, 9034–9038 (2017).
60. Díaz, S. A. et al. Extending DNA-based molecular photonic wires with homogeneous förster resonance energy transfer. *Adv. Opt. Mater.* **4**, 399–412 (2016).
61. Liu, J., Guillemeney, L., Abécassis, B. & Coolen, L. Long range energy transfer in self-assembled stacks of semiconducting nanoplatelets. *Nano Lett.* **20**, 3465–3470 (2020).
62. Craig, D. P. & Thirunamachandran, T. Molecular Quantum Electrodynamics: An Introduction to Radiation Molecule Interactions; Academic Press Press (London) Inc. Ltd: London, UK, (1984).
63. Georgiadou, D. G. et al. High responsivity and response speed single-layer mixed-cation lead mixed-halide perovskite photodetectors based on nanogap electrodes manufactured on large-area rigid and flexible substrates. *Adv. Funct. Mater.* **29**, 1901371 (2019).
64. Wang, F. et al. Fully depleted self-aligned heterosandwiched van der waals photodetectors. *Adv. Mater.* **34**, 2203283 (2022).
65. Munkhbat, B., Wróbel, P., Antosiewicz, T. J. & Shegai, T. O. Optical constants of several multilayer transition metal dichalcogenides measured by spectroscopic ellipsometry in the 300–1700 nm range: high index, anisotropy, and hyperbolicity. *ACS Photonics* **9**, 2398–2407 (2022).

Acknowledgments

This work is supported by the Strategic Priority Research Program of the Chinese Academy of Sciences (Grant No. XDB0580000 (W. H.)), National Natural Science Foundation of China (Grant Nos. T2521003 (W. H.), 62334011 (J.M.), 62261136552 (J.M.), 62005303 (J.M.), 62134001 (J.M.), and 51925208 (W. H.)), National Key Research and Development Program of China (Grant Nos. 2021YFA0715602 (J.M.) and 2023YFB3611400 (W. H.)), CAS Project for Young Scientists in Basic Research (Grant No. YSBR-113 (J.M.)), and Shanghai Youth Elite Sailing Program (23YF1455200 (H. G.)). A.A. recognizes full support for this work from the Vagelos Institute for Energy Science and Technology Graduate Student Fellowship. D.J. acknowledges partial support for this work from the Sloan Fellowship in Chemistry.

Author contributions

W.H., J.M. and D.J. conceived the idea and directed the collaboration and execution. Q.Z. and M.X. fabricated the devices and performed the measurements. Q.Z., W.H., D.J., J.M., A.A., R.X., L.S, M.X., F.W., and A.G. analyzed the experimental data. Q.Z., A.A., and H.G. did the calculations and simulations. Q.Z., A.A., D.J., J.M., and W.H. co-wrote the manuscript with contributions from all the authors. All authors discussed the results and implications and commented on the manuscript.

Competing interests

The authors declare no competing interests.

Additional information

Supplementary information The online version contains supplementary material available at https://doi.org/10.1038/s41467-026-68312-8.

Correspondence and requests for materials should be addressed to Deep Jariwala, Jinshui Miao or Weida Hu.

Peer review information *Nature Communications* thanks the anonymous reviewers for their contribution to the peer review of this work. A peer review file is available.